Room-temperature spin-orbit torque in NiMnSb

C. Ciccarelli,[1, a)] L. Anderson,[1, a)] V. Tshitoyan,[1] A. J. Ferguson,[1, b)] F. Gerhard,[2]
C. Gould,[2] L. W. Molenkamp,[2] J. Gayles,[3] J. Železný,[4, 5] L. Šmejkal,[4, 5] Z. Yuan,[3]
J. Sinova,[3, 4] F. Freimuth,[6] and T. Jungwirth[4, 7]

[1)] *Cavendish Laboratory, University of Cambridge, CB3 0HE,*
United Kingdom

[2)] *Physikalisches Institut (EP3), Universität Würzburg, Am Hubland,*
D-97074 Würzburg, Germany

[3)] *Institut für Physik, Johannes Gutenberg Universität Mainz, 55128 Mainz,*
Germany

[4)] *Institute of Physics, Academy of Sciences of the Czech Republic, Cukrovarnicka 10,*
162 00 Praha 6, Czech Republic

[5)] *Faculty of Mathematics and Physics, Charles University in Prague, Ke Karlovu 3,*
121 16 Prague 2, Czech Republic

[6)] *Peter Grünberg Institut and Institute for Advanced Simulation,*
Forschungszentrum Jülich and JARA, 52425 Jülich, Germany

[7)] *School of Physics and Astronomy, University of Nottingham,*
Nottingham NG7 2RD, United Kingdom

(Dated: 19 May 2016)

[a)]These authors have contributed equally to the work.

[b)]e-mail: ajf1006@cam.ac.uk

Materials that crystalize in diamond-related lattices, with Si and GaAs as their prime examples, are at the foundation of modern electronics. Simultaneously, inversion asymmetries in their crystal structure and relativistic spin-orbit coupling led to discoveries of non-equilibrium spin-polarization phenomena that are now extensively explored as electrical means for manipulating magnetic moments in a variety of spintronic structures. Current research of these relativistic spin-orbit torques focuses primarily on magnetic transition-metal multilayers. The low temperatures diluted magnetic semiconductor (Ga,Mn)As, in which spin-orbit torques were initially discovered, has to date remained the only example showing the phenomenon among bulk non-centrosymmetric ferromagnets. Here we present a general framework, based on the complete set of crystallographic point groups, for identifying the potential presence and symmetry of spin-orbit torques in non-centrosymmetric crystals. Among the candidate room-temperature ferromagnets we choose for our experiments NiMnSb which is a member of the broad family of magnetic Heusler compounds. By performing all-electrical ferromagnetic resonance measurements in single-crystal epilayers of NiMnSb we detect room-temperature spin-orbit torques generated by effective fields of the expected Dresselhaus symmetry and of magnitude consistent with our ab initio calculations.

Recently, the focus of spintronic research has been on phenomena which exploit the relativistic transfer between the linear momentum of the electron and spin. The spin Hall effect (SHE) and the inverse spin galvanic effect (ISGE), experimentally discovered more than a decade ago as companion phenomena in GaAs based structures[1–5], play a fundamental role in this so called spin-orbitronics research field. Unlike the SHE generating a uniform spin-current and a resulting surface/interface spin accummulation, the ISGE induces directly a uniform non-equilibrium spin polarization in spin-orbit coupled crystals with broken inversion symmetry. The ISGE (also called the Edelstein effect) was experimentally discovered[2–4,6,7] in GaAs whose bulk zinc-blende unit cell is non-centrosymmetric.

The non-equilibrium spin polarization generated by the ISGE and the corresponding effective field can induce spin-orbit torques on the magnetization in non-centrosymmetric magnetic crystals, as demonstrated in the low Curie temperatures diluted magnetic semiconductor (Ga,Mn)As[8–11], or in magnetic multilayers with structural inversion asymmetry[12–15].

The multilayers, typically comprising an interface of a high Curie temperature transition metal ferromagnet and a strongly spin-orbit coupled paramagnet, have attracted most of the attention to date for their direct relevance to magnetic memory and other spintronic applications. However, the single-layer magnets we focus on in this work have their own merits in the research of current induced spin-orbit torques. The effects in these systems originate from the ISGE and corresponding broken symmetries of bulk crystals while in the magnetic multilayers the ISGE mechanism is entangled with the SHE[13–16]. The understanding of spin-orbit torques in bulk non-centrosymmetric crystals is therefore more straightforward and their potentially utility in spintronic devices is more robust against unintentional disorder and structural imperfections than the spin-orbit coupling phenomena generated within a few atomic planes near the ferromagnet/paramagnet interface.

Since the low Curie temperature disordered alloy (Ga,Mn)As has to date been the only studied material in which spin-orbit torques are generated by the bulk ISGE we start this paper with a general analysis of the potential presence and of symmetries of the ISGE-induced spin-orbit fields considering all 21 crystal point groups with broken inversion symmetry. This opens the route for exploring and potentially exploiting spin-orbit torques in non-centrosymmetric crystals beyond the singular and academic example of (Ga,Mn)As. We then identify NiMnSb as a candidate ferromagnet for observing the spin-orbit torque in an ordered magnetic crystal at room temperature.

NiMnSb is a member of the broad family of magnetic Heusler compounds which in bulk is predicted to be a half-metal ferromagnet and has a Curie temperature of 730 K[17,18]. The material can have a low Gilbert damping constant $\sim 10^{-3}$ and tuneable magnetic anisotropies when grown in thin films[19]. For these characteristics, NiMnSb has been utilized in earlier spintronics studies of non-relativistic magneto-transport and spin dynamics effects based on spin angular momentum transfer between carriers and magnetization in magnetic-multilayer devices[20,21]. In the second part of our paper we report experiments in single-crystal epilayers of NiMnSb in which we identify the ISGE-induced spin-orbit torques by employing the all-electrical ferromagnetic resonance (FMR) technique[10,11,16,22,23]. Experimental results are compared with *ab initio* transport theory calculations of the spin-orbit torque in the studied NiMnSb material.
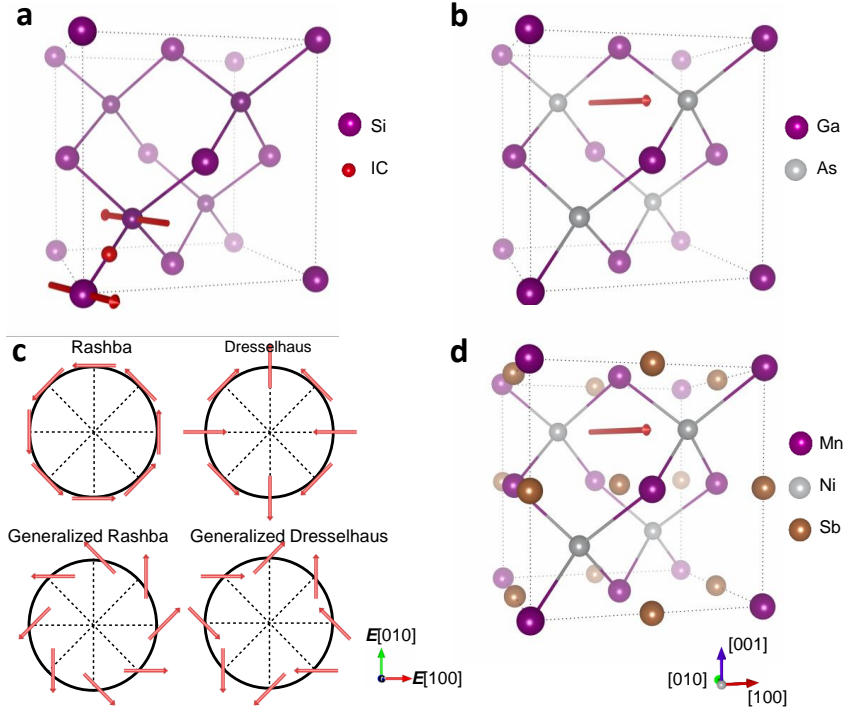
FIG. 1. Relativistic non-equilibrium spin polarizations in non-centorsymmetric lattices. (a) Crystal unit cell of Si. The red dot indicates the inversion center (IC) of the unit cell. In this case, the inversion partners are occupied by the same atomic species. By symmetry, the local current-induced spin polarization (red arrows) has the same magnitude and opposite sign on the two inversion partner sites, which results in a zero global spin polarization. (b) Crystal unit cell of GaAs. In this case the inversion partners are occupied by different atomic species, which makes the unit cell globally non-centrosymmetric and results in a non-zero net spin polarization. (c) Rashba, Dresselhaus, and generalized Rashba and Dresselhaus symmetries of the non-equilibrium spin polarization with respect to the crystal direction of the applied electric field that can occur in different non-centrosymmetric crystals listed in Tab. 1. (d) Crystal unit cell of half-Heusler NiMnSb. The symmetry of the cell is analogous to that of GaAs shown in (b).

Symmetry analysis of spin-orbit fields in non-centrosymmetric crystals

In Figs. 1a,b we illustrate examples of the relativistic non-equilibrium spin polarizations that occur in the family of diamond-related lattices for the case when the two inversion partner lattice sites of the unit cell are occupied by the same or by different atomic species. The ISGE responsible for these polarization effects requires the spin-orbit coupling to be

4

combined with inversion asymmetries in the crystal structure[24,25]. Each of the two atomic lattice sites in the unit cell of the crystals shown in Fig. 1a,b have inversion asymmetric local environment[26] which allows for the generation of the local current-induced spin polarizations[27,28].

point group	field-like χ	point group	field-like χ
2	$\begin{pmatrix} x_{11} & 0 & x_{13} \\ 0 & x_{22} & 0 \\ x_{31} & 0 & x_{33} \end{pmatrix}$	312	$\begin{pmatrix} x_{11} & 0 & 0 \\ 0 & x_{11} & 0 \\ 0 & 0 & x_{33} \end{pmatrix}$
m	$\begin{pmatrix} 0 & x_{12} & 0 \\ x_{21} & 0 & x_{23} \\ 0 & x_{32} & 0 \end{pmatrix}$	3m1	$\begin{pmatrix} 0 & -x_{21} & 0 \\ x_{21} & 0 & 0 \\ 0 & 0 & 0 \end{pmatrix}$
222	$\begin{pmatrix} x_{11} & 0 & 0 \\ 0 & x_{22} & 0 \\ 0 & 0 & x_{33} \end{pmatrix}$	6	$\begin{pmatrix} x_{11} & -x_{21} & 0 \\ x_{21} & x_{11} & 0 \\ 0 & 0 & x_{33} \end{pmatrix}$
mm2	$\begin{pmatrix} 0 & x_{12} & 0 \\ x_{21} & 0 & 0 \\ 0 & 0 & 0 \end{pmatrix}$	-6	$\begin{pmatrix} 0 & 0 & 0 \\ 0 & 0 & 0 \\ 0 & 0 & 0 \end{pmatrix}$
4	$\begin{pmatrix} x_{11} & -x_{21} & 0 \\ x_{21} & x_{11} & 0 \\ 0 & 0 & x_{33} \end{pmatrix}$	622	$\begin{pmatrix} x_{11} & 0 & 0 \\ 0 & x_{11} & 0 \\ 0 & 0 & x_{33} \end{pmatrix}$
-4	$\begin{pmatrix} x_{11} & x_{21} & 0 \\ x_{21} & -x_{11} & 0 \\ 0 & 0 & 0 \end{pmatrix}$	6mm	$\begin{pmatrix} 0 & -x_{21} & 0 \\ x_{21} & 0 & 0 \\ 0 & 0 & 0 \end{pmatrix}$
422	$\begin{pmatrix} x_{11} & 0 & 0 \\ 0 & x_{11} & 0 \\ 0 & 0 & x_{33} \end{pmatrix}$	-6m2	$\begin{pmatrix} 0 & 0 & 0 \\ 0 & 0 & 0 \\ 0 & 0 & 0 \end{pmatrix}$
4mm	$\begin{pmatrix} 0 & -x_{21} & 0 \\ x_{21} & 0 & 0 \\ 0 & 0 & 0 \end{pmatrix}$	23	$\begin{pmatrix} x_{11} & 0 & 0 \\ 0 & x_{11} & 0 \\ 0 & 0 & x_{11} \end{pmatrix}$
-42m	$\begin{pmatrix} x_{11} & 0 & 0 \\ 0 & -x_{11} & 0 \\ 0 & 0 & 0 \end{pmatrix}$	432	$\begin{pmatrix} x_{11} & 0 & 0 \\ 0 & x_{11} & 0 \\ 0 & 0 & x_{11} \end{pmatrix}$
3	$\begin{pmatrix} x_{11} & -x_{21} & 0 \\ x_{21} & x_{11} & 0 \\ 0 & 0 & x_{33} \end{pmatrix}$	-43m	$\begin{pmatrix} 0 & 0 & 0 \\ 0 & 0 & 0 \\ 0 & 0 & 0 \end{pmatrix}$

TABLE I. Current-induced spin-orbit field symmetries for all point groups with broken inversion symmetry. x_{ij} denotes a component of the response tensor χ. The tensor for the triclinic group 1 is not shown, since its form is completely arbitrary. The tensors are given in cartesian coordinate systems, see the Supplementary Information for details on how these coordinate systems are chosen for each point group. The tensors are given in conventional coordinate systems defined in the International Tables for Crystallography[37].

By symmetry, the global polarization vanishes when integrated over the entire unit cell if the two sites are occupied by the same atom since the unit cell has an inversion center (highlighted by a red dot in Fig. 1a). Only local current-induced polarizations of the same magnitude and opposite sign at the two inversion-partner sites remain non-zero in this case (red arrows in Fig. 1a). When the sites are occupied by different atoms, the unit cell is globally inversion asymmetric allowing for the generation of a net global spin polarization with a non-zero integral value over the unit cell (rad arrow in Fig. 1b). For completeness we point out that in these diamond-related cubic lattices an additional symmetry lowering has

to be introduced to allow for the above non-equilibrium polarization effects. For example, in thin films with tetragonal distortion due to a substrate lattice-matching strain, the current induced spin polarization acquires a Dresselhaus symmetry with respect to the crystal direction of the applied current[9–11], illustrated in Fig. 1c. A shear strain, on the other hand, generates spin polarization with the Rashba symmetry[10,11] (see Fig. 1c).

In Tab. 1 we summarize symmetries of the current-induced spin polarizations and the corresponding spin-orbit fields, $\mathbf{h} = \chi\mathbf{E}$, based on the analysis of all crystals belonging to the 21 point groups with broken inversion symmetry. Here $\mathbf{E}$ is the applied electric field and χ is the response tensor. To find this tensor for each point group we used the Neumann's principle, i.e., we looked for axial tensors which satisfy $\chi = \det(R)R\chi R^{-1}$ for all symmetry operations R (for more details see Sec. 4 in Supplementary information). The resulting current-induced spin-orbit field symmetries with respect to the applied electric field direction are of the generalized Rashba or Dressehaus form shown in Fig. 1c, or the spin-orbit field is parallel to $\mathbf{E}$, or the symmetries are a combination of these three forms.

The cubic half-Heusler lattice of NiMnSb, shown in Fig. 1d, shares the -43m point-group symmetry with the cubic diamond (zinc-blende) lattices. Under a tetragonal distortion, corresponding e.g. to the lattice-matching growth strain, the symmetry of these crystals reduces to -42m. As seen from Tab. 1, the current-induced polarization is non-zero in the -42m point group and has the Dresselhaus symmetry.

Measurements of spin-orbit fields in NiMnSb

In order to deduce the vector of the current-induced effective field in NiMnSb, we perform current driven ferromagnetic resonance (FMR) measurements on two-terminal micro-bars, similarly to previous investigations in spin-valves,[22] in ferromagnet/paramagnet bilayers,[23] and to our previous experiments in (Ga,Mn)As[10,11].

Our samples consist of an insulating InP substrate, 200 nm of an $In_{0.53}Ga_{0.47}As$ buffer lattice-matched to the substrate and 37 nm of a fully strained NiMnSb film capped with 5 nm of MgO. The material was grown in a multi-chamber molecular-beam-epitaxy system, allowing for transfer between different chambers under ultra-high vacuum.[19] The crystal quality of the epilayers was confirmed by high resolution X-ray diffraction and RHEED measurements. 4 μm$\times$40 μm bars are patterned by electron beam lithography and ion
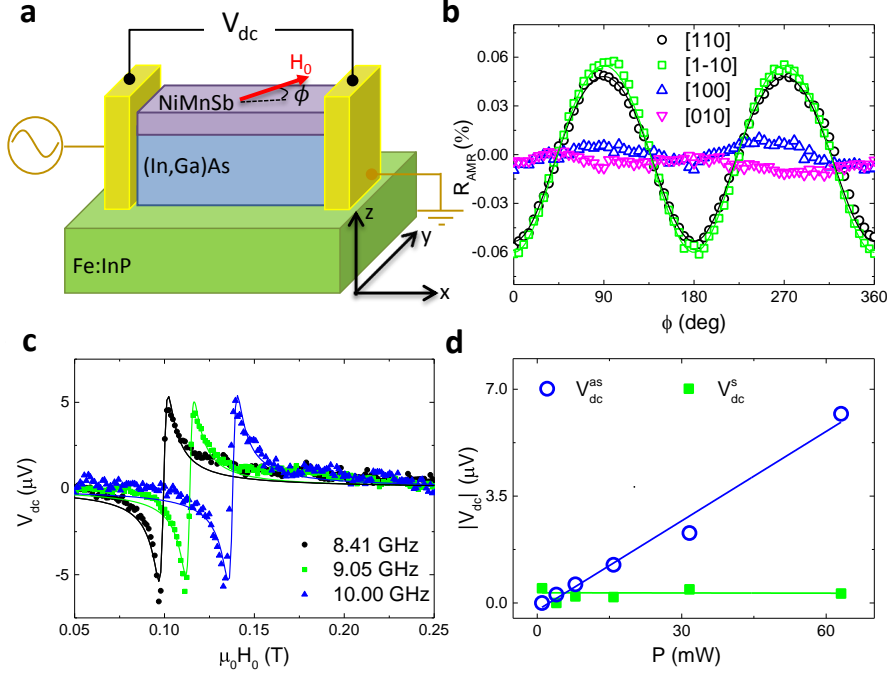
6

FIG. 2. Spin-orbit FMR experiment. (a) Schematic of the sample and measuring set-up. 4×40 μm^2 bars are patterned from (In,Ga)As/NiMnSb epilayers on an insulating Fe-doped InP substrate. A microwave current is passed in the bar and excites spin-orbit FMR. By measuring the longitudinal dc voltage we are able to deduce the amplitude of precession, thus the magnitude of the spin-orbit driving field. The angle ϕ is the angle between the current flow and the external field around which the magnetization precesses. (b) AMR measured in the [110], [1$\bar{1}$0], [100], and [010] oriented bars. (c) The rectified voltage showing FMR for different frequencies of the microwave current in a bar along the [110] direction. The Lorentzians are well fitted by an antisymmetric line-shape (continuous line) at all frequencies. (d) Power dependence of the symmetric and antisymmetric components of the rectified voltage.

milling.

The measurement set-up is shown in Fig. 2a. All measurements presented in this work were performed at room temperature using an electromagnet to generate the magnetic field H_0 and a rotating stage to set its direction ϕ with respect to the bar. The magnetization of NiMnSb is initially aligned along H_0. When an alternating electrical current $I(t) = Ie^{i\omega t}$ is passed through the uniformly magnetized micro-bar, carriers gain a non-equilibrium spin polarization due to the ISGE. This spin-polarization is exchange coupled to the magnetization
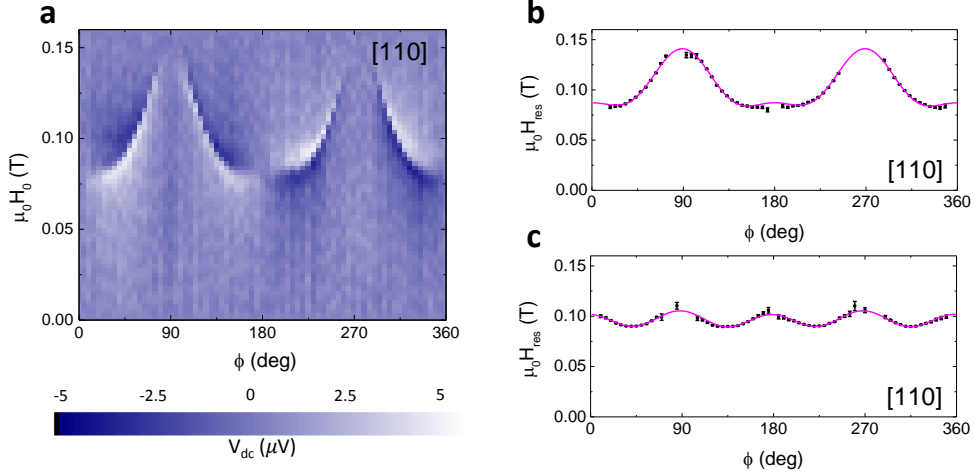
FIG. 3. Angle dependence of the resonance field. (a) Rectified voltage measured for a bar oriented along the [110] crystal direction as a function of the external field's amplitude and direction. (b)-(c) Resonance field measured for a bar along the [110] crystal axis (b) and along the [1-10] crystal axis (c) as a function of the angle ϕ. The continuous line represents the fitting with the modified Kittel's formula (2). The error bars in $\mu_0 H_{res}$ represent the fitting error obtained by fitting the resonance in V_{dc} with a linear combination of symmetric and antisymmetric Lorentzians.

At resonance, the precessing motion of the magnetization induces a time-dependent change of the bar longitudinal resistance owing to anisotropic magneto-resistance (AMR). Fig. 2b shows static measurements of the AMR in bars patterned along [110], [1$\bar{1}$0], [100], and [010] crystal directions. We define $R_{AMR} \equiv \frac{R(\phi) - \bar{R}}{\bar{R}}$ where R is the longitudinal resistance and $\bar{R}$ is the longitudinal resistance averaged over ϕ. For the [110] and [1$\bar{1}$0] oriented bars, $R_{AMR} \approx C \cos(2\phi)$ where $C \approx 0.06\%$. At resonance, the resistance oscillates with amplitude $dR_{AMR} \approx -2C \sin(2\phi)d\phi$, where $d\phi$ is the precessional amplitude, directly proportional to the torque in the limit of small oscillations.

The product between the oscillating resistance and the oscillating current in the bar yields a rectified component of the longitudinal voltage, $V_{dc} = < dR_{AMR}(t) \times I(t) >_t$, where $< * >_t$ refers to a time-average, which is measured via a bias-tee. By solving the Landau$-$Lifshitz$-$Gilbert equation for an arbitrarily oriented current-induced field, we find that at resonance the rectified voltage is the linear combination of symmetric and anti-symmetric Lorentzians, which depend on the components of the field as[10,11]:

8

$$V_{dc}^{sym} = JCA_{sym}\sin(2\phi)h_z \tag{1}$$

$$V_{dc}^{asym} = JCA_{asym}\sin(2\phi)[-h_x\sin(\phi) + h_y\cos(\phi)]$$

A_{sym} and A_{asym} are constants determined by the magnetic anisotropy, while h_x, h_y and h_z are the components of the current-induced field in the coordinate system specified in Fig. 2a. We note that the $\sin(2\phi)$ term derives from the angle dependence of dR_{AMR}, whereas the $\sin(\phi)$ and $\cos(\phi)$ terms in V_{dc}^{asym} express the angle dependence of the torque.

Only bars oriented along the [110] and [1$\bar{1}$0] axes were used in the FMR experiments. The AMR in [100] and [010] oriented bars nearly vanishes, as seen in Fig. 2b, and cannot produce rectification. In the Supplementary information we explain, based on symmetry analysis of the AMR measurements and on *ab initio* AMR calculations, that this is a consequence of the cancellation of non-crystalline and crystalline AMR terms in the NiMnSb film. Nevertheless, FMR measurements in the [110] and [1$\bar{1}$0] oriented bars are sufficient for inferring the magnitude and symmetry of the driving spin-orbit fields.

Fig. 2c shows V_{dc} for a bar along the [110] crystal direction as the external magnetic field is swept through the FMR condition at different angles to the bar. The resonance is well fitted by an antisymmetric Lorentzian. The independence of the line-shape on the frequency of the current indicates that the phase between the current passed in the bar and the current-induced driving field is fixed and is not affected by reactive components of the circuit.[29] This is a necessary requirement to carry the line-shape analysis outlined in Refs. 10 and 11. The amplitude of the resonance is proportional to the incident microwave power (see Fig. 2d) implying that the driving field is linear in current density, as is typical for most mechanisms of current induced torques, including the Oersted field torque and the spin torques.

Fig. 3a shows the complete angle analysis of the rectified voltage for a bar along the [110] crystal axis. In these measurements the frequency of the current is fixed at $\omega = 2\pi \cdot 9$ GHz, with a source power of 20 dBm. A resonance is clearly visible at fields above the saturation field of 30 mT. The resonance field depends on the anisotropy of the bar and its angle dependence can be fitted with the modified Kittel's formula deduced from the expression of the free energy[10,30–32] (for details see Supplementary Information), which at magnetic fields larger than the saturation field reads:
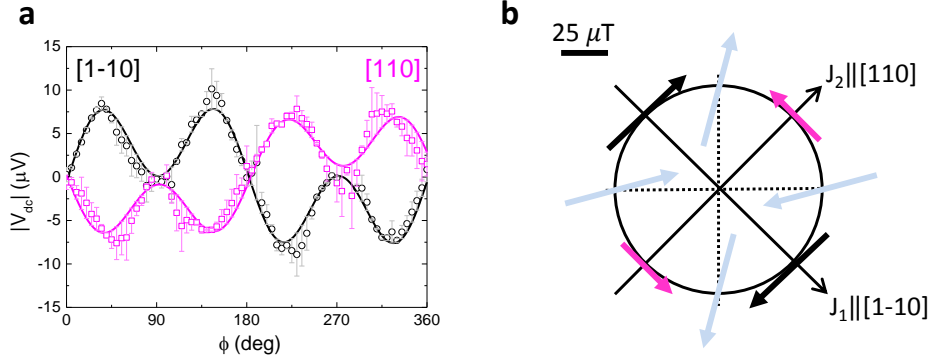
FIG. 4. Spin-orbit field components.(a) Antisymmetric component of the resonance in the rectified voltage for a bar along the [110] crystal axis (magenta squares) and a bar along the [1-10] crystal axis (black circles). From the fitting with equation (1), represented by the continuous line, we obtain magnitude and direction of the spin-orbit field for current flowing along the [110] direction, $\mathbf{h}_{[110]}$, and the [1-10] direction, $\mathbf{h}_{[1-10]}$. (b) Polar plot illustrating the direction of the spin-orbit field for current flowing along different crystal directions of NiMnSb. The fields represented by the magenta and black arrows were experimentally obtained. The fields represented by the light blue arrows were deduced by using $\mathbf{h}_{[110]}$ and $\mathbf{h}_{[1-10]}$ as an orthogonal basis.

$$\left(\frac{\omega}{\gamma}\right)^2 = H_1 H_2 \tag{2}$$

where:

$$H_1 = \mu_0[H_{res} + H_{4\parallel}\cos 4\theta - H_{2\parallel}\sin 2\theta]$$

$$H_2 = \mu_0[H_{res} + \frac{H_{4\parallel}}{4}(3 + \cos 4\theta) + H_{2\parallel}(1 - \sin 2\theta) + M_{eff}]$$

$\mu_0 H_{res}$ is the resonance field, $\mu_0 H_{2\parallel}$ and $\mu_0 H_{4\parallel}$ are the in-plane uniaxial and biaxial anisotropy fields, $M_{eff} = M_s - \mu_0 H_{2\perp}$ is the effective magnetization, M_s being the saturation magnetization and $\mu_0 H_\perp$ the out-of-plane anisotropy field, while θ is the angle of the external magnetic field and magnetization with the [100] crystal direction, with $\theta = \phi + \frac{\pi}{4}$ for bars along the [110] crystal axis and $\theta = \phi - \frac{\pi}{4}$ for bars along the [1-10] crystal axis.

By rearranging equation (2), we find an expression for H_{res} as a function of ϕ. Fig. 3b and c show the fitting obtained for the two crystal directions by using this expression. From the fitting we extract the values of the anisotropy fields, treated as free parameters:

10

$\mu_0 H_{2\perp}^{110} = 638 \pm 3$ mT and $\mu_0 H_{2\perp}^{1-10} = 640 \pm 3$ mT, $\mu_0 H_{2\|}^{110} = 21.4 \pm 0.3$ mT and $\mu_0 H_{2\|}^{1-10} = 0.1 \pm 0.4$ mT, and $\mu_0 H_{4\|}^{110} = 11.1 \pm 0.5$ mT and $\mu_0 H_{4\|}^{1-10} = 7.2 \pm 0.5$ mT. The out-of-plane uniaxial anisotropy field induced by the lattice-matching growth strain is the leading term. Note that the in-plane anisotropies are different in the two micro-bars since their values in the unpatterned film are modified differently by partial ($\sim 10\%$) strain relaxation in the 4 μm wide bars[10]. The Gilbert damping constant inferred from the dependence of the FMR line-width on frequency is $(1.8 \pm 0.10) \times 10^{-3}$, in agreement with previous reports[19] (see Supplementary Information).

In Fig. 4a we plot the amplitude of the resonance with respect to the angle ϕ for the [110] and [1$\bar{1}$0] oriented bars. In both cases the amplitude exhibits a $\sin(2\phi)\cos(\phi)$ dependence, indicating maximum amplitude of precession, thus maximum torque, when the external magnetic field is aligned with the bar. By fitting these graphs with the expression (1) for V_{dc} we determine the value of the current-induced fields: $h_{[110]} = (340 \pm 20)$ μT and $h_{[1\bar{1}0]} = (-550 \pm 50)$ μT normalised to a current density $J = 10^7$ Acm^{-2} (the current density was deduced by heating calibration measurements as detailed in the Supplementary Information).

The current-induced fields measured for the two bars have opposite sign, excluding the Oersted field as a possible driving mechanism of precession and confirming their crystal origin. Fig. 4b shows the complete polar plot of the current-induced field in our bars, constructed by using the measured values $h_{[110]}$ (magenta arrow) and $h_{[1\bar{1}0]}$ (black arrow) as an orthogonal basis. The polar plot is well described by a predominant Dresselhaus field $h_D = (445 \pm 54)$ μT and a smaller Rashba field $h_R = (105 \pm 54)$ μT. Similarly to (Ga,Mn)As, we attribute the Rashba contribution to sheer strain in the unpatterned films, which also accounts for the uniaxial term of the magnetic anisotropy,[10,19,33] combined with partial strain relaxation in the patterned bars.

Measurements on multiple sets of samples patterned along the [110] and [1$\bar{1}$0] crystal directions provided reproducible evidence for a room-temperature field-like torque driven by an effective field with the leading Dresselhaus symmetry.

Microscopic calculations of spin-orbit fields in NiMnSb

To obtain a theoretical estimate of the magnitude of the effective field which drives the spin-orbit torque in our NiMnSb film we performed relativistic density-functional-theory (DFT) calculations using two complementary approaches. In one method[34] we base our calculations on the full-potential linearized augmented plane-wave DFT code FLEUR for the description of the electronic structure. The spin-orbit torque is then calculated using the Kubo formalism for the linear response of the torque operator to the electric field. Effects of disorder are approximated by a constant quasiparticle broadening. In another method,[35,36] the electronic structure is determined in the DFT framework based on the tight-binding linear muffin-tin orbital approach. In the torque calculation, a scattering region is constructed with the desired disorder and connected to semi-infinite perfectly crystalline leads. The non-equilibrium spin polarization that is carried by conduction electrons is obtained from the explicit scattering wave functions using the wave function matching scheme. Thermal disorder is treated in the frozen phonon approximation. More details on these *ab initio* methods are given in the Supplementary Information.

In both calculations we considered the symmetry-lowering mechanism of the bulk cubic lattice of NiMnSb due to the substrate-matching growth strain. The resulting current-induced fields are of the Dresselhaus symmetry, in agreement with the crystallographic point group analysis and with experiment. The magnitude of the current-induced field obtained by the two *ab initio* methods is 89 and 111 μT per $J = 10^7$ Acm^{-2}, respectively. Without any adjustable parameter, the theoretical results agree on the order of magnitude level with our experiments.

Conclusion

To conclude, we have presented a general framework, based on the complete set of crystallographic point groups, for identifying the potential occurrence and symmetry of current induced spin-orbit fields in non-centrosymmetric crystals. Based on these general arguments we have searched for a ferromagnetic crystal in which the spin-orbit torques can be detected at room temperature. We have identified NiMnSb for its globally non-centrosymmetric crystal structure reminiscent of GaAs, for its high ferromagnetic Curie temperature, and a range

of other favorable structural and magnetic properties. By performing room-temperature electrical FMR measurements in NiMnSb epilayers, we have detected current induced effective fields of the theoretically expected Dresselhaus symmetry and of a magnitude consistent with microscopic *ab initio* calculations. This has implications beyond designing spintronic devices in NiMnSb. Our results can guide the search for other favorable room temperature magnets that can be switched by the internal current-induced spin-orbit fields and do not require for the switching external magnetic fields or auxiliary polarizers embedded in complex magnetic multilayer structures.

I. METHODS

A. Materials

The 37-nm-thick NiMnSb epilayer (room temperature conductivity of 2×10^4 Ω^{-1} cm^{-1}) was grown on 200 nm In$_{0.53}$Ga$_{0.47}$As buffer layer (room temperature conductivity of 0.1 Ω^{-1} cm^{-1}) and Fe:InP insulating substrate and capped with 5 nm of MgO. The vertical lattice constant of 5.951 $\mathring{A}$ indicates a slightly Ni-rich composition.

B. Experimental procedure

A pulse-modulated (at 880 Hz) microwave signal was launched onto a printed circuit board patterned with a coplanar waveguide and then injected into the sample via a bond wire. The rectified voltage, generated at FMR, was separated from the microwave circuit by using a bias tee, amplified with a voltage amplifier and then detected with a lock-in amplifier. All measurements were performed at room temperature. A rotating stage allowed setting the orientation of the bar with respect to the fixed in-plane magnetic field generated by an electro-magnet.

REFERENCES

[1] Y. K. Kato, R. C. Myers, A. C. Gossard, and D. D. Awschalom, "Observation of the spin Hall effect in semiconductors." Science **306**, 1910–1913 (2004).

[2] Y. K. Kato, R. Myers, A. Gossard, and D. D. Awschalom, "Current-Induced Spin Polarization in Strained Semiconductors," Phys. Rev. Lett. **93**, 176601 (2004).

[3] J. Wunderlich, B. Kaestner, J. Sinova, and T. Jungwirth, "Experimental discovery of the spin-Hall effect in Rashba spin-orbit coupled semiconductor systems," arXiv:cond-mat/0410295v1 (2004).

[4] J. Wunderlich, B. Kaestner, J. Sinova, and T. Jungwirth, "Experimental observation of the spin-Hall effect in a two dimensional spin-orbit coupled semiconductor system," Phys. Rev. Lett. **94**, 047204 (2005).

[5] J. Sinova, S. O. Valenzuela, J. Wunderlich, C. H. Back, and T. Jungwirth, "Spin Hall effect," Rev. Mod. Phys. **87**, 1213–1259 (2015).

[6] A. Y. Silov, P. A. Blajnov, J. H. Wolter, R. Hey, K. H. Ploog, and N. S. Averkiev, "Current-induced spin polarization at a single heterojunction," Appl. Phys. Lett. **85**, 5929 (2004).

[7] S. D. Ganichev, S. N. Danilov, P. Schneider, V. V. Bel'kov, L. E. Golub, W. Wegscheider, D. Weiss, and W. Prettl, "Can an electric current orient spins in quantum wells?" arXiv:cond-mat/0403641 (2004).

[8] B. A. Bernevig and S.-C. Zhang, "Spin splitting and spin current in strained bulk semiconductors," Phys. Rev. B **72**, 115204 (2005).

[9] A. Chernyshov, M. Overby, X. Liu, J. K. Furdyna, Y. Lyanda-Geller, and L. P. Rokhinson, "Evidence for reversible control of magnetization in a ferromagnetic material by means of spinorbit magnetic field," Nat. Phys. **5**, 656–659 (2009).

[10] D. Fang, H. Kurebayashi, J. Wunderlich, K. Výborný, L. P. Zârbo, R. P. Campion, A. Casiraghi, B. L. Gallagher, T. Jungwirth, and A. J. Ferguson, "Spin-orbit-driven ferromagnetic resonance." Nat. Nanotechnol. **6**, 413–7 (2011).

[11] H. Kurebayashi, J. Sinova, D. Fang, A. Irvine, T. D. Skinner, J. Wunderlich, V. Novák, R. P. Campion, B. L. Gallagher, E. K. Vehstedt, L. P. Zârbo, K. Výborný, A. J. Ferguson, and T. Jungwirth, "An antidamping spin-orbit torque originating from the Berry curvature." Nat. Nanotechnol. **9**, 211–7 (2014).

[12] A. Manchon and S. Zhang, "Theory of nonequilibrium intrinsic spin torque in a single nanomagnet," Phys. Rev. B **78**, 212405 (2008).

[13] I. M. Miron, K. Garello, G. Gaudin, P.-J. Zermatten, M. V. Costache, S. Auffret, S. Bandiera, B. Rodmacq, A. Schuhl, and P. Gambardella, "Perpendicular switching of a single ferromagnetic layer induced by in-plane current injection." Nature **476**, 189–193 (2011).

[14] L. Liu, C.-F. Pai, Y. Li, H. W. Tseng, D. C. Ralph, and R. A. Buhrman, "Spin-torque switching with the giant spin Hall effect of tantalum." Science **336**, 555–558 (2012).

[15] K. Garello, I. M. Miron, C. O. Avci, F. Freimuth, Y. Mokrousov, S. Blügel, S. Auffret, O. Boulle, G. Gaudin, and P. Gambardella, "Symmetry and magnitude of spin-orbit torques in ferromagnetic heterostructures." Nat. Nanotechnol. **8**, 587–93 (2013).

[16] T. D. Skinner, K. Olejnik, L. K. Cunningham, H. Kurebayashi, R. P. Campion, B. L. Gallagher, T. Jungwirth, and A. J. Ferguson, "Complementary spin-Hall and inverse spin-galvanic effect torques in a ferromagnet/semiconductor bilayer," Nat. Commun. **6**,

6730 (2015).

[17]M. J. Otto, R. A. M. V. Woerden, P. J. V. D. Valk, J. Wijngaard, C. F. V. Bruggen, C. Haas, and K. H. J. Buschow, "Half-metallic ferromagnets : I . Structure and magnetic properties of NiMnSb and related inter-metallic compounds," J. Phys. Condens. Matter **1**, 2341–2350 (1989).

[18]M. J. Otto, R. a. M. V. Woerden, P. J. V. D. Valk, J. Wijngaard, C. F. V. Bruggen, and C. Haas, "Half-metallic ferromagnets. II. Transport properties of NiMnSb and related inter-metallic compounds," J. Phys. Condens. Matter **1**, 2351–2360 (1999).

[19]F. Gerhard, C. Schumacher, C. Gould, and L. W. Molenkamp, "Control of the magnetic in-plane anisotropy in off-stoichiometric NiMnSb," J. Appl. Phys. **115**, 094505 (2014).

[20]C. Hordequin, J. P. Nozières, and J. Pierre, "Half metallic NiMnSb-based spin-valve structures," J. Magn. Magn. Mat. **183**, 225–231 (1998).

[21]A. Riegler, *Ferromagnetic resonance study of the Half-Heusler alloy NiMnSb: The benefit of using NiMnSb as a ferromagnetic layer in pseudo spin-valve based spin-torque oscillators*, Ph.D. thesis, Universitaet Wuerzburg (2011).

[22]a. a. Tulapurkar, Y. Suzuki, A. Fukushima, H. Kubota, H. Maehara, K. Tsunekawa, D. D. Djayaprawira, N. Watanabe, and S. Yuasa, "Spin-torque diode effect in magnetic tunnel junctions." Nature **438**, 339–42 (2005).

[23]L. Liu, T. Moriyama, D. C. Ralph, and R. A. Buhrman, "Spin-Torque Ferromagnetic Resonance Induced by the Spin Hall Effect," Phys. Rev. Lett. **106**, 036601 (2011).

[24]E. L. Ivchenko and S. D. Ganichev, "Spin-photogalvanic," in *Spin Phys. Semicond.*, edited by M. Dyakonov (Springer, New York, 2008) p. 245.

[25]V. V. Belkov and S. D. Ganichev, "Magneto-gyrotropic effects in semiconductor quantum wells," Semicond. Sci. Technol. **23**, 114003 (2008).

[26]X. Zhang, Q. Liu, J.-W. Luo, A. J. Freeman, and A. Zunger, "Hidden spin polarization in inversion-symmetric bulk crystals," Nat. Phys. **10**, 387–393 (2014).

[27]J. Železný, H. Gao, K. Výborný, J. Zemen, J. Mašek, A. Manchon, J. Wunderlich, J. Sinova, and T. Jungwirth, "Relativistic Néel-Order Fields Induced by Electrical Current in Antiferromagnets," Phys. Rev. Lett. **113**, 157201 (2014).

[28]P. Wadley, B. Howells, J. Elezny, C. Andrews, V. Hills, R. P. Campion, V. Novak, K. Olejnik, F. Maccherozzi, S. S. Dhesi, S. Y. Martin, T. Wagner, J. Wunderlich, F. Freimuth, Y. Mokrousov, J. Kune, J. S. Chauhan, M. J. Grzybowski, A. W. Rushforth, K. W. Ed-

monds, B. L. Gallagher, and T. Jungwirth, "Electrical switching of an antiferromagnet," Science , 14 January (2016).

[29]M. Harder, Z. X. Cao, Y. S. Gui, X. L. Fan, and C.-M. Hu, "Analysis of the line shape of electrically detected ferromagnetic resonance," Phys. Rev. B **84**, 054423 (2011).

[30]J. O. Artman, "Ferromagnetic resonance in metal single crystals," Phys. Rev. **105**, 74–84 (1957).

[31]J. Artman, "Microwave resonance relations in anisotropic single crystal ferrites," Proceedings of the IRE **44**, 1284–1293 (1956).

[32]M. Farle, "Ferromagnetic resonance of ultrathin metallic layers," Reports on Progress in Physics **61**, 755 (1998).

[33]A. Koveshnikov, G. Woltersdorf, J. Q. Liu, B. Kardasz, O. Mosendz, B. Heinrich, K. L. Kavanagh, P. Bach, A. S. Bader, C. Schumacher, C. Rster, C. Gould, G. Schmidt, L. W. Molenkamp, and C. Kumpf, "Structural and magnetic properties of nimnsb/ingaas/inp(001)," Journal of Applied Physics **97**, 073906 (2005), http://dx.doi.org/10.1063/1.1873036.

[34]F. Freimuth, S. Blügel, and Y. Mokrousov, "Spin-orbit torques in Co/Pt(111) and Mn/W(001) magnetic bilayers from first principles," Phys. Rev. B **90**, 174423 (2014).

[35]K. Xia, M. Zwierzycki, M. Talanana, P. J. Kelly, and G. E. W. Bauer, "First-principles scattering matrices for spin transport," Phys. Rev. B **73**, 064420 (2006).

[36]Y. Liu, A. a. Starikov, Z. Yuan, and P. J. Kelly, "First-principles calculations of magnetization relaxation in pure Fe, Co, and Ni with frozen thermal lattice disorder," Phys. Rev. B **84**, 014412 (2011).

[37]T. Hahn, ed., *International Tables for Crystallography*, 1st ed., Vol. A (Chester: International Union of Crystallography, 2006).

Acknowledgments

Author contributions

Theory and data modelling were performed by J.G., J.Z., L.S., Z.Y., J.S., F.F. and T.J. Materials were prepared by F.G. and C.G. Sample preparation was performed by C.C. Experiments and data analysis were carried out by C.C., L.A., V.T. and A.F. The manuscript was written by T.J.and C.C., project planning was performed by A.J.F., L.W.M., J.S. and T.J. All authors discussed the results and commented on the paper.

Competing Financial Interests

The authors declare no competing financial interests.